Dynamics of bubbles under stochastic pressure forcing

Riccardo Vesipa,[1,*] Eleonora Paissoni,[2] Costantino Manes,[1] and Luca Ridolfi[1]
[1]*Department of Environment, Land and Infrastructure Engineering, Politecnico di Torino, C. so Duca degli Abruzzi 24, 10129 Torino, Italy*
[2]*Cranfield Water Science Institute, Cranfield University, Bedfordshire MK43 0AL, United Kingdom*

(Received 24 July 2020; accepted 28 January 2021; published 23 February 2021)

Several studies have investigated the dynamics of a single spherical bubble at rest under a nonstationary pressure forcing. However, attention has almost always been focused on periodic pressure oscillations, neglecting the case of stochastic forcing. This fact is quite surprising, as random pressure fluctuations are widespread in many applications involving bubbles (e.g., hydrodynamic cavitation in turbulent flows or bubble dynamics in acoustic cavitation), and noise, in general, is known to induce a variety of counterintuitive phenomena in nonlinear dynamical systems such as bubble oscillators. To shed light on this unexplored topic, here we study bubble dynamics as described by the Keller-Miksis equation, under a pressure forcing described by a Gaussian colored noise modeled as an Ornstein-Uhlenbeck process. Results indicate that, depending on noise intensity, bubbles display two peculiar behaviors: when intensity is low, the fluctuating pressure forcing mainly excites the free oscillations of the bubble, and the bubble's radius undergoes small amplitude oscillations with a rather regular periodicity. Differently, high noise intensity induces chaotic bubble dynamics, whereby nonlinear effects are exacerbated and the bubble behaves as an amplifier of the external random forcing.

DOI: 10.1103/PhysRevE.103.023108

I. INTRODUCTION

Over the past few decades, the dynamics of gas-bubbles (also referred to as cavities) in liquids has attracted a lot of interest in the scientific community; see, e.g., [1–3]. This paper focuses on the canonical case of a spherical bubble subjected to a prescribed external forcing which drives variations in the bubble's radius. The problem has been extensively addressed (see, e.g., [4–7]) and can be mathematically described by ordinary differential equations, which, depending upon different simplifying assumptions, can take different forms [8–12]. Despite such differences, all these equations share the common feature of retaining strongly nonlinear terms which make gas-bubbles in liquids dynamically rich systems [13].

One of the attractive features of bubble dynamics involves the possibility of cavities undergoing abrupt variations in size. In particular, due to the high inertia of the liquid hosting the cavities, bubbles, if properly excited, can be subjected to abrupt collapses that generate intense pressure and temperature peaks, which, in turn, are associated with the generation of shock waves and the emission of light and sound [14–16].

The attractiveness of such extreme pressure and temperature events stems from the fact that they can be exploited in several technological applications. For instance, in medicine, bubble collapses are used to break liver and kidney stones and cancer cells [17,18]. In the water industry, bubbles' collapses physically inactivate bacteria, and the free-radicals generated by the temperature peaks reached during the collapsing phase are used to oxidize pollutants for waste-water treatment purposes [19–22]; in geophysics, bubble implosions are useful for subsea geological explorations [23,24].

Several factors influence bubble dynamics. The most relevant are the properties of the liquid hosting the gas bubble [25], the presence of solid boundaries close to the bubble [26–28], the interaction with other proximal gas cavities [29,30], and the action of an external forcing that alters the bubble equilibrium conditions. Two classes of forcing are commonly considered. The first one consists in the alteration of the bubble size in a liquid at rest (with time-invariant pressure) using either laser beams or sparks [31,32]. The second class involves variations of the static pressure of the liquid hosting the bubble [33,34]. Static pressure variations are usually induced by ultrasound waves traveling within a volume of liquid at rest [35,36] or by alterations of the liquid velocity (e.g., geometrical constrictions like orifice plates or Venturi tubes) in a pressurized system of conduits [37,38].

The pressure forcing—especially the case of pressure fluctuations in a liquid at rest—has been the focus of a great deal of studies and will be considered also in the present paper. Most previous works have generally explored the effects of sinusoidal pressure oscillations on the bubble's radius (see, e.g., [39]). In spite of the simple and regular temporal structure of the forcing, the response of the bubble turned out to be very rich, exhibiting period-doubling bifurcations and period-doubling cascades that can ultimately lead to a chaotic behavior [40–45].

Other studies have investigated the forced dynamics of bubbles when the pressure of the hosting liquid is perturbed by a biharmonic signal obtained as the sum of two sinusoidal signals [46,47]. It was found that such a combined signal induces significant alterations in the thresholds of period-doubling bifurcations and period-doubling cascades. It was

*riccardo.vesipa@polito.it

therefore suggested to adopt biharmonic pressure signals to control chaos inception and to give a more controlled and predictable bubble behavior [48]. Finally, some theoretical and experimental studies have focused on the transient phase occurring during the inception of an ultrasound field and in pulsed ultrasound fields [49–51]. Results showed that the collapse of bubbles was more intense in the transient phases, rather than during the regular sinusoidal phase of pulsed ultrasound fields.

In the authors' opinion, the aforementioned results from the literature suggest that transients and irregularities of the external forcing can lead to yet unexplored bubbles' responses. This should not be entirely surprising because it is well known that many interesting and unexpected phenomena emerge from the stochastic forcing (i.e., a form of irregular forcing) of strongly nonlinear systems (i.e., the so called noise-induced phenomena; see [52–55]). It is within this context that the aim and relevance of the present paper are cast. The aim is indeed to explore the response of a single bubble to random fluctuations of the external pressure. The relevance of the study lies in the fact that stochastic pressure-forcing is important for a number of applications, and is encountered in a number of environments. Notable examples include (i) hydrodynamic cavitation reactors (mainly used for water-treatment processes) where the pressure fluctuations imposed by turbulence and by the geometry of the reactor are known to heavily influence bubble dynamics [30,43,56] and, ultimately, bubble efficiency in oxidation and disinfection processes; and (ii) acoustic cavitation reactors, where bubble dynamics is influenced by the interactions between the sinusoidal pressure-waves generated by ultrasound transmitters and the random shock pressure waves generated by imploding bubbles [38,57,58].

To fulfill the aim of the paper, we chose to adopt a modeling approach whereby the dynamics of bubble was investigated through numerical integration of the Keller-Miksis equations [40]. The pressure of the fluid hosting the bubble (i.e., the pressure forcing) was assumed to undergo stochastic fluctuations which were simulated using the Ornstein-Uhlenbeck model [59]. This model is well-established and represents a wide number of random processes in nature [60–63]. More importantly, it is characterized by only two free parameters that allow for a systematic exploration of noise-intensity and noise-autocorrelation effects on bubble dynamics.

II. METHODS

A. Mathematical modeling of bubble dynamics

We focus on a single bubble located far from solid boundaries or liquid surfaces. The bubble is assumed to be spherical, positionally stable, and its surface is assumed not to be affected by instability mechanisms [64]. To study the dynamics of this type of cavity, it is standard to focus on the temporal evolution of the bubble radius, $R(t)$, where t is time. A well-known mathematical framework for the modeling of $R(t)$ is given by the Keller-Miksis equation [40]

$$\left(1-\frac{\dot{R}}{c}\right)R\ddot{R}+\left(1-\frac{\dot{R}}{3c}\right)\frac{3}{2}\dot{R}^2=\left(1+\frac{\dot{R}}{c}\right)\left(\frac{p_w-p(t)}{\rho}\right)+\frac{R}{c}\frac{d}{dt}\left(\frac{p_w-p(t)}{\rho}\right), \tag{1}$$

where dots denote time derivation, c is the speed of sound, ρ is the liquid density, $p(t)$ is the (possibly time-dependent) liquid pressure indefinitely far from the bubble wall (often indicated in the literature also as p_∞), and p_w is the liquid pressure at the bubble wall. We chose the Keller-Miksis equation in place of more simplified formulations (e.g., the Rayleigh-Plesset equation) in order to properly model large and fast temporal variations of the radius $R(t)$ [40]. In the following, we will show that long-lasting and large increments of the bubbles' radius play a key role in determining chaos in the radius dynamics. In this regard, Nazari-Mahroo *et al.* [65] compared the Keller-Miksis, Gilmore, and Lezzi-Prosperetti models, and showed that—during the radius expansion stage—they behave very similarly. This means that the results presented herein are robust and overall insensitive to the choice of the specific bubbles' dynamics model. It should also be noted that during the radius expansion stage, the bubble remains spherical. This is confirmed, for instance, by the experiments reported by Löfstedt *et al.* [66].

The bubble is assumed to contain a mixture of liquid vapor and noncondensible gas and to be submerged within a liquid at constant temperature. If this mixture behaves as an ideal gas, the total pressure inside the bubble can be evaluated as $p_G + p_v$, where p_G and p_v are the gas and vapor partial pressure inside the cavity, respectively. Under this assumption, the pressure at the bubble wall, p_w, can be derived by a force balance at the gas-liquid interface, reading

$$p_w = p_G + p_v - \frac{2S}{R} + 4\mu\frac{\dot{R}}{R}, \tag{2}$$

where S is the surface tension, and μ is the liquid dynamic viscosity. Provided that the liquid that hosts the bubble is kept at a constant temperature, the vapor pressure inside the cavity, p_v, is also constant. The gas pressure inside the bubble, instead, can be evaluated according to the polytropic relationship

$$p_G = p_{G,\mathrm{eq}}\left(\frac{R_{\mathrm{eq}}}{R}\right)^{3k}, \tag{3}$$

where $p_{G,\mathrm{eq}}$ and R_{eq} are the gas pressure inside a bubble and the bubble radius in equilibrium conditions, respectively, and k is the so-called polytropic exponent. In this study, bubbles are supposed to undergo adiabatic volume changes, i.e., $k = 1.4$. This is consistent with several studies [3,67,68] that have shown that bubble dynamics—as predicted by adiabatic mathematical models—matches experimental observations. Finally, the pressure inside a bubble in steady conditions,

TABLE I. Physical parameters adopted for the liquid hosting the bubble. Data refer to water at 293 K.

ρ (kg m^{-3})	S (N m^{-1})	μ (Pa s)	c (m s^{-1})	p_v (Pa)
998	73×10^{-3}	1.00×10^{-3}	1481	2338

$p_{G,\mathrm{eq}}$, is evaluated from (1) and (2) setting $\dot{R} = \ddot{R} = 0$ as

$$p_{G,\mathrm{eq}} = p - p_v + \frac{2S}{R_{\mathrm{eq}}}, \tag{4}$$

where p is the pressure of the liquid far from the bubble.

A key parameter is the period of bubble-free oscillations [3,25]

$$T_n = 2\pi \left(\frac{3k(p - p_v)}{\rho R_{\mathrm{eq}}^2} + \frac{2(3k-1)S}{\rho R_{\mathrm{eq}}^3} \right)^{-\frac{1}{2}}. \tag{5}$$

This parameter will be crucial in the interpretation of the temporal evolution of the cavity radius $R(t)$. In the following, water at 293 K is assumed as the hosting liquid, and Table I reports the corresponding physical parameters.

B. The stochastic forcing

The pressure of the liquid hosting the bubble is supposed to evolve over time as

$$p(t) = \bar{p} + p'(t), \tag{6}$$

where $\bar{p}$ is the mean pressure experienced by the cavity, and $p'(t)$ is the time-dependent fluctuation around $\bar{p}$. The fluctuations $p'(t)$ are modeled as an Ornstein-Uhlenbeck process [59,63].

The Ornstein-Uhlenbeck process is a stationary colored Gaussian-Markov process with the following characteristics: (i) the probability density function of the realizations $p'(t)$ is a normal distribution with zero mean and standard deviation σ_p; (ii) the stochastic process is exponentially autocorrelated as $\overline{p'(t)p'(t+\tau)} = \sigma_p \exp[-\tau/\tau_p]$, where τ_p is the autocorrelation timescale; and (iii) the process is stationary, namely σ_p and τ_p do not change over time.

We have chosen the Ornstein-Uhlenbeck process as the random pressure forcing due to its simplicity, mathematical tractability, and the possibility of changing its variance and (linear) memory by acting on only two parameters, namely the standard deviation σ_p and the autocorrelation timescale τ_p.

From a numerical point of view, the realizations of the pressure fluctuations, $p'(t)$, are evaluated by the so-called "exact update formula" provided by Gillespie [69], namely

$$p'(t + \Delta t) = p'(t)\zeta + \sigma_p \sqrt{1 - \zeta^2} n, \tag{7}$$

where n is a unit normal random number, Δt is the time step of the process, and $\zeta = \exp[-\Delta t/\tau_p]$. Since (7) provides an exact update for $p'(t)$, the actual value of the time step of the process is arbitrary, and $\Delta t = \tau_p/50$ was chosen in this study.

C. Simulation of bubble radius dynamics

To investigate the effect of the stochastic pressure forcing on the dynamics of a bubble [i.e., on the time-series of the bubble radius $R(t)$], a number of numerical simulations were performed. Each numerical simulation consisted of two steps. First, a random pressure forcing $p(t)$ was simulated according to (7). Secondly, Eq. (1) was forced with $p(t)$ and numerically solved to obtain the response of the bubble, namely the time-series of the radius $R(t)$.

Simulations of $p(t)$ were performed setting $\bar{p} = 100 \times 10^3$ Pa. Three correlation times $\tau_p = [0.5, 1, 2]T_n$ were considered, and the standard deviation of the pressure was changed in the range $[0, 120] \times 10^3$ Pa. The duration of the simulations was set equal to $4000T_n$. This duration guaranteed a robust estimation of all the statistical properties of $R(t)$ for all the investigated conditions.

To obtain $R(t)$ from the numerical integration of (1) with the forcing (7), the initial conditions $R(0) = R_{\mathrm{eq}} = 5 \times 10^{-6}$ m and $\dot{R}(0) = \ddot{R}(0) = 0$ were imposed and the time step $\Delta t = 10^{-8}$ s was adopted. $R(t)$ was normalized with the equilibrium radius R_{eq} [25,40,45] to better quantify the dynamics of the bubble radius.

Figure 1(b) reports the time-series of the normalized radius $R(t)/R_{\mathrm{eq}}$ as obtained from integration of Eq. (1) when forced with the pressure reported in Fig. 1(a). In Figs. 1(c) and 1(d), the PDFs of the time-series $p(t)$ and $R(t)$ [partially reported in panels (a) and (b)] illustrate the variability of $p(t)$ and $R(t)$. Similarly, Figs. 1(e) and 1(f) report the autocorrelation functions, and illustrate how the correlation time is evaluated.

The interested reader can find in Appendix C further details about the numerical techniques adopted to solve (1) and a sensitivity analysis of the solution with respect to the time step adopted for the numerical solution, the duration of the simulations, and the number of realizations adopted for the statistical analyses.

III. RESULTS

Four complementary perspectives are adopted to study the behavior of $R(t)/R_{\mathrm{eq}}$. The first (Sec. III A) is based on bifurcation diagrams and presents a way to identify the onset of chaos in the $R(t)/R_{\mathrm{eq}}$ time-series. The second (Sec. III B) investigates the physical mechanisms underpinning the onset of chaotic fluctuations. The third (Sec. III C) is a detailed statistical analysis of $R(t)/R_{\mathrm{eq}}$, with a particular emphasis on the dependence of $R(t)/R_{\mathrm{eq}}$ statistical moments on various combinations of noise intensity and correlation timescales. Finally, Sec. III D digs deeper into second-order statistics and investigates dominant modes and characteristic timescales of $R(t)/R_{\mathrm{eq}}$ time-series. This provides hints about the random versus organized temporal structure of $R(t)$.

All the results are wrapped up in Sec. IV, which provides an overview of the bubbles' behavior under stochastic pressure forcing, using and harmonizing all the results obtained from Secs. III A–III D.

A. Assessment of the temporal pattern and bifurcation diagram

We begin the results section by discussing the temporal dynamics exhibited by $R(t)/R_{\mathrm{eq}}$. To this aim, the values $R(t =$

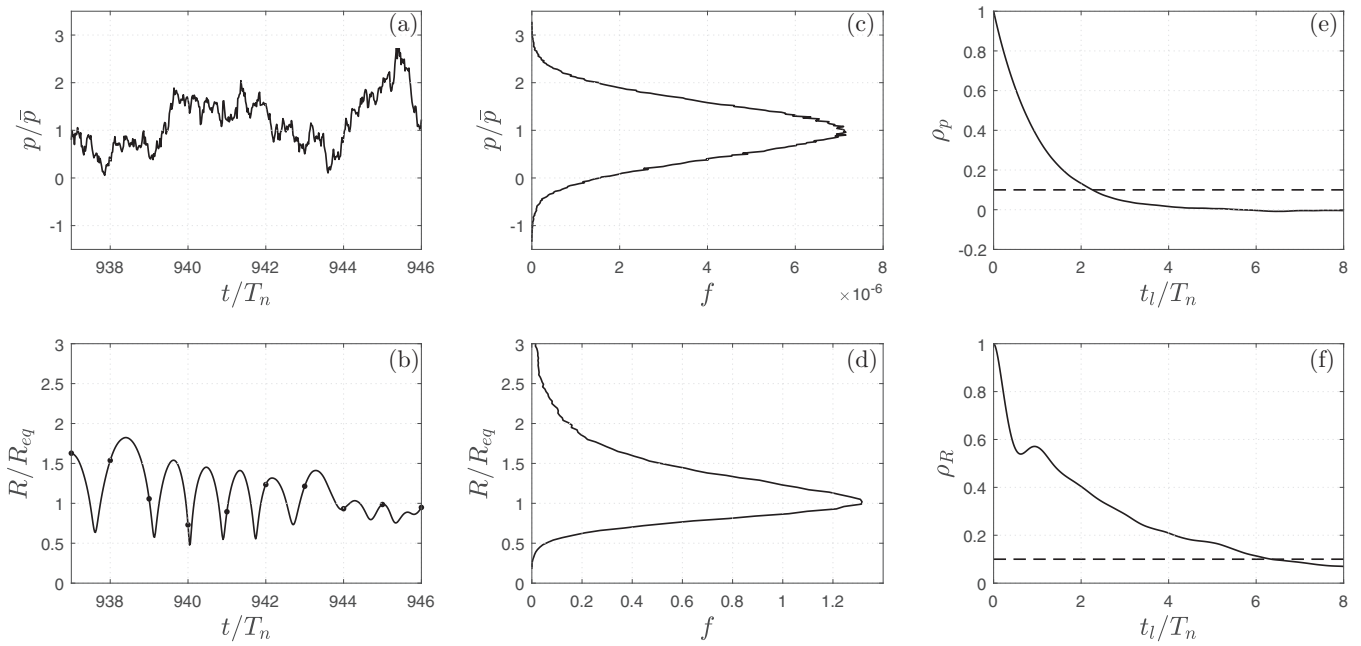

FIG. 1. (a) Example of a time-series of the normalized stochastic pressure forcing $p(t)/\bar{p}$. (b) Time-series of the normalized radius $R(t)/R_{\rm eq}$ of the bubble forced by the pressure reported in (a). The black dots in (b) highlight the bubble radius attained at the instants nT_n, where n is an integer and T_n is the natural oscillation period of the bubble (see Sec. III A for the explanation). (c),(d) Probability density functions, and (e),(f) autocorrelation functions of the time-series (partially) reported in (a) and (b). The dashed lines in (e) and (f) mark the level $\rho_p = \rho_R = 0.1$. It should be noted that the time-lag $\hat{t}_l$ such that $\rho(\hat{t}_l) = 0.1$ is defined as the correlation time of the time-series. The times in (a) and (b) and the time lags reported in (e) and (f) are normalized by T_n. The adopted parameters are $\sigma_p = 60 \times 10^3$ Pa and $\tau_p = 2.0T_n = 2.8 \times 10^{-6}$ s.

$nT_n)/R_{\rm eq}$ with $n = 1, 2, \ldots$ were extracted from $R(t)/R_{\rm eq}$ [see the dot symbols in Fig. 1(b)]. If the bubble radius oscillation exhibits a period T_n, $R(t)$ takes the same value at instants that are multiples of T_n. Conversely, if $R(t)$ is not periodic (or when the period of oscillations is different from T_n), then $R(nT_n)/R_{\rm eq}$ exhibits a variability.

Figures 2(a) and 2(b) show results associated with the analysis of $R(nT_n)/R_{eq}$ in the form of noise-intensity bifurcation diagrams. These graphs report on the noise intensity $\sigma_p/\bar{p}$ (on the x-axis) and on the values of $R(nT_n)/R_{\rm eq}$ (on the y-axis) extracted from the corresponding time-series $R(t)$. The gray and red dots in Figs. 2(a) and 2(b) refer to different correlation times τ_p. The noise-intensity-bifurcation diagrams obtained in Figs. 2(a) and 2(b) align with those obtained from other studies that considered a sinusoidal forcing [25,40,45], but key differences can be observed.

In the case of a sinusoidal forcing with amplitude A_p and period T_n, the noise-intensity-bifurcation diagrams exhibit two different zones. When A_p is lower than a threshold $A_{p,c}$, the metric $R(nT_n)/R_{\rm eq}$ is perfectly constant for any n. This can be seen, for example, in Figs. 3(a) and 3(b), which report the radius dynamics forced by the sinusoidal pressure with amplitude $A_p < A_{p,c}$ shown in Figs. 3(d) and 3(e). Differently, for $A_p > A_{p,c}$ the metric $R(nT_n)/R_{\rm eq}$ exhibits a large variability for a fixed value of A_p and for different values of n. This nonregular behavior is exemplified in Fig. 3(c), which shows the radius dynamics under the sinusoidal pressure forcing with amplitude $A_p > A_{p,c}$ of Fig. 3(f). Therefore, in the case of a sinusoidal forcing, $A_{p,c}$ represents an amplitude threshold that sharply separates the nonchaotic and chaotic regimes.

When stochastic fluctuations of pressure are considered, the variability of $R(nT_n)/R_{\rm eq}$ increases with increasing $\sigma_p/\bar{p}$ [Figs. 2(a) and 2(b)]. This is consistent with the case of a sinusoidal forcing. However, while $\sigma_p/\bar{p}$ increases, a clear threshold that separates regular oscillations from chaotic fluctuations does not emerge. Moreover, even for very low values of $\sigma_p/\bar{p}$, the metric $R(nT_n)/R_{\rm eq}$ does show some level of variability and hence it is not constant.

A more careful inspection shows that a change in the bubble dynamics occurs at $\sigma_p/\bar{p} \approx 0.30$: for $\sigma_p/\bar{p} \lessapprox 0.30$, the normalized radius oscillates around 1 and is confined by the almost symmetrical curves $\exp[1.9(\sigma_p/\bar{p})]$ and $\exp[-1.5(\sigma_p/\bar{p})]$ [these curves were obtained by fitting the maximum and minimum values attained by $R(nT_n)/R_{\rm eq}$ for $\sigma_p/\bar{p} < 0.30$]; differently, for $\sigma_p/\bar{p} \gtrapprox 0.30$, the variability of the radius suddenly increases and $R(nT_n)/R_{\rm eq} \in [0.01, 50]$.

B. Physics of chaos inception

To elucidate the physical behavior behind the inception of chaos in the dynamics of $R(t)$ occurring for $\sigma_p/\bar{p} > 0.3$, Figs. 2(c) and 2(d) report two exemplifying portions of time-series $R(t)/R_{\rm eq}$. To relate the bubble radius dynamics to the pressure fluctuations, the corresponding time-series $p(t)/\bar{p}$ are reported in Figs. 2(e) and 2(f). These pressure time-series are obtained setting the same noise timescale $\tau_p = T_n$ but different noise intensities. The dotted lines mark the threshold $p(t)/\bar{p} = 1$, and they help to discern the instants when the instantaneous forcing pressure is below average [i.e., $p(t)/\bar{p} < 1$] or above average [i.e., $p(t)/\bar{p} > 1$]. We recall that when the

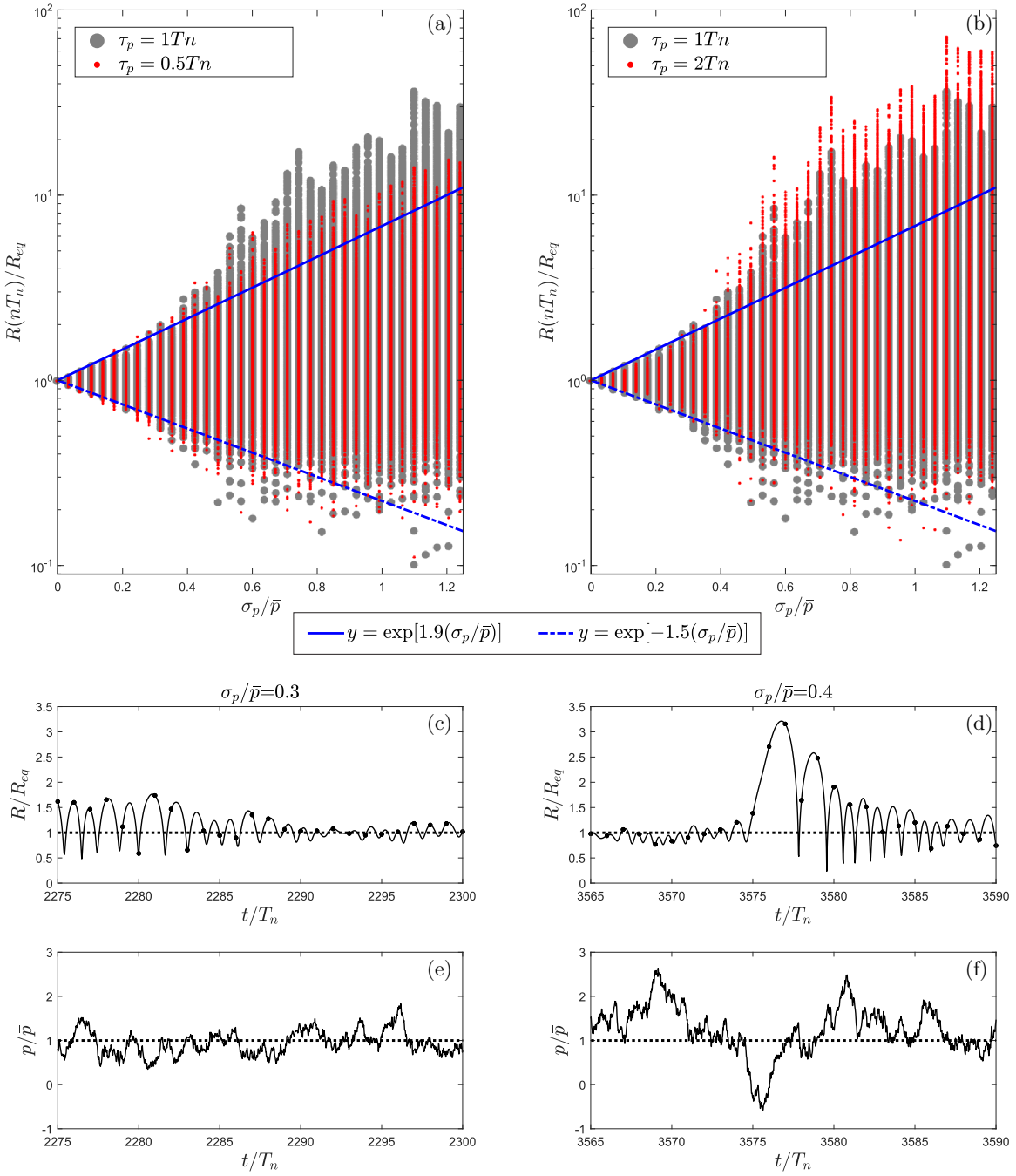

FIG. 2. (a),(b) Noise-intensity bifurcation diagrams. For a given value of $\sigma_p/\bar{p}$, the dynamics of $R(t)$ is simulated for $4000T_n$. From this simulation, only the values $R(nT_n)/R_{\rm eq}$ are selected, and they are reported in the vertical axis for the given $\sigma_p/\bar{p}$. In both panels, the gray circles refer to $\tau_p = T_n$. In panels (a) and (b), the red dots refer to $\tau_p = T_n/2$ and $\tau_p = 2T_n$, respectively. (c)–(f) Time segments of the time-series $R(t)/R_{\rm eq}$ and $p(t)/\bar{p}$. The horizontal dotted lines mark the equilibrium radius $R(t)/R_{\rm eq} = 1$ and the mean pressure $p(t)/\bar{p} = 1$. The black dots in (c) and (d) highlight the bubble radius attained at the instants nT_n. Panels (c) and (e) refer to $\sigma_p/\bar{p} = 0.3$, and panels (d) and (f) refer to $\sigma_p/\bar{p} = 0.4$; in both cases, $\tau_p = T_n$.

instantaneous pressure is below (above) average, the bubble radius tends to increase (decrease).

Figures 2(c) and 2(e) refer to the noise intensity $\sigma_p/\bar{p} = 0.3$ (i.e., just below the threshold that separates the nonchaotic/chaotic behaviors). In this case, the pressure oscillates slightly around the mean value [Fig. 2(e)] and the bubble radius does not undergo large increments [$R(t)/R_{\rm eq}$ never exceeds the value 2; see Fig. 2(c)]. It follows that during the small radius increments, little energy is stored in the bubble. As a consequence of this, (i) the subsequent rebound is mild [$R(t)/R_{\rm eq}$ remains close to unity], and (ii) the radius growth that follows the rebound is mild as well. The radius dynamics is therefore characterized by a sequence of modest increments of radius intercut with mild rebounds. At these conditions, the period of the oscillations is very close to the natural oscillation period of the bubble and no chaos is detected.

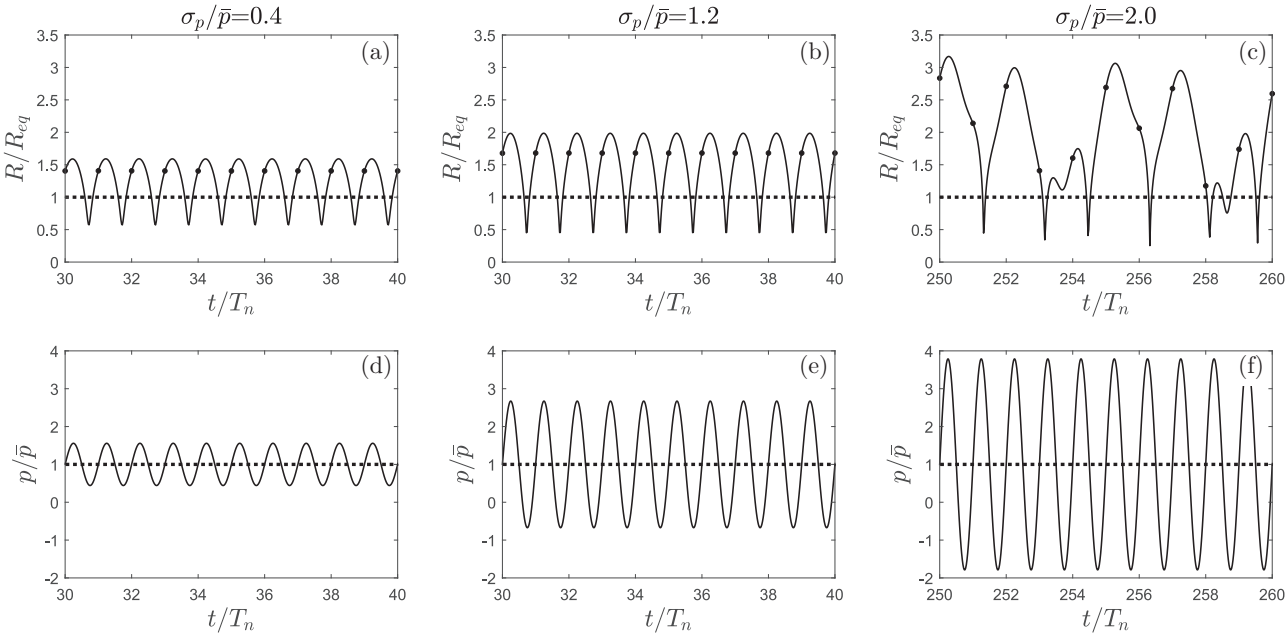

FIG. 3. Time segments of the time-series $R(t)/R_{\rm eq}$ (top row) and $p(t)/\bar{p}$ (bottom row) when a sinusoidal external pressure—with amplitude $A_p = \sqrt{2}\sigma_p$ and period $\tau_p = T_n$—is applied. The dotted lines mark the equilibrium radius $R(t)/R_{\rm eq} = 1$ and the mean pressure $p(t)/\bar{p} = 1$. The black dots in (a)–(c) highlight the bubble radius attained at the instants nT_n. Panels (a),(d), (b),(e), and (c),(f) refer to $\sigma_p/\bar{p} = 0.4$, $\sigma_p/\bar{p} = 1.2$, and $\sigma_p/\bar{p} = 2.0$, respectively.

In contrast, Figs. 2(d) and 2(f) focus on the noise intensity $\sigma_p/\bar{p} = 0.4$ (i.e., above the no-chaos/chaos threshold). In this case, the pressure may deviate significantly from the mean value [e.g., see immediately after $t/T_n = 3575$ in Fig. 2(f)]. As a result, large increments in the bubble radius occur, which may last a few times the natural period T_n. For instance, this can be seen in Fig. 2(d), where the radius growth starting at $t/T_n \approx 3575$ lasts about $3T_n$, and $R(t)/R_{\rm eq}$ eventually exceeds the value 3. During these large increments of radius, a significant amount of energy is stored in the bubble. Consequently, (i) the subsequent rebound is violent [$R(t)/R_{\rm eq}$ is much lower than unity], and (ii) the radius growth that follows the rebound may be considerable and long-lasting [this is exemplified in Fig. 2(d), where the radius growth that begins after the rebound at $t/T_n \approx 3578$ lasts about $2T_n$]. The radius dynamics is therefore characterized by a sequence of significant and long-lasting increments of radius (the duration of these phases exhibit a wide variability) intercut with violent rebounds. At these conditions, $R(t)/R_{\rm eq}$ deviates significantly from unity, and the period of the oscillations varies significantly from the natural oscillation period of the bubble. Accordingly, a chaotic behavior is detected. It should be noted that the behaviors reported in the time segments of Figs. 2(c)–2(f) are not rare, but they are detected in a large number of time segments in the time-series simulated in this work.

The examples previously reported depict a picture where bubble chaotic dynamics is characterized by long-lasting and large radius increments, induced by time-coherent negative pressure fluctuations. It follows that chaos occurs when downcrossing events in the pressure signal exceed suitable thresholds, namely, the duration and the magnitude of the negative pressure fluctuations (with respect to the pressure mean value) become sufficiently high. In the cases investigated in this work, such downcrossing analysis shows that bubble chaotic dynamics occurs when (i) the duration of pressure reduction events exceeds the threshold $1.5T_n$, and (ii) the corresponding mean value of the pressure reduction during these negative pressure events is greater than $0.6\bar{p}$. However, it should be noted that the bubble response to pressure forcing depends on the physical properties of fluid and the initial size of the bubble. Therefore, the physics of chaos inception previously described (i.e., the interplay between long-lasting, intense pressure fluctuations and nonlinear bubble dynamics) is of general validity. However, the exact threshold values dictating the transition to chaos detected here are surely dependent on the fluid characteristics (see Table I). The precise determination of this dependence is beyond the scope of the present work, and will be the subject of future work.

We now briefly highlight the key role of pressure stochasticity in the inception of chaos in bubble dynamics. To this aim, we evaluated the response of a bubble to three sinusoidal pressure forcings $p(t)/\bar{p} = 1 + (A_p/\bar{p})\sin(2\pi t/T_n)$, and we compared it against the behavior depicted in Figs. 2(d) and 2(f). Three relevant values of the oscillation amplitude, A_p, were tested: (i) $A_p/\bar{p} = \sqrt{2} \times 0.4$, such that the standard deviation of the sinusoidal signal is $\sigma_p = 0.4 \times \bar{p}$, and the resulting radius dynamics can be compared with Fig. 2(d) (that refers to a stochastic pressure forcing with $\sigma_p/\bar{p} = 0.4$); (ii) $A_p/\bar{p} = \sqrt{2} \times 1.2$ (i.e., the sinusoidal forcing is characterized by $\sigma_p/\bar{p} = 1.2$) such that the minimum pressure attained by the sinusoidal forcing is the same as that typically attained by the stochastic forcing of Fig. 2(f); and (iii) $A_p/\bar{p} = \sqrt{2} \times 2.0$, inducing pressure oscillations with $\sigma_p/\bar{p} = 2.0$, i.e., much

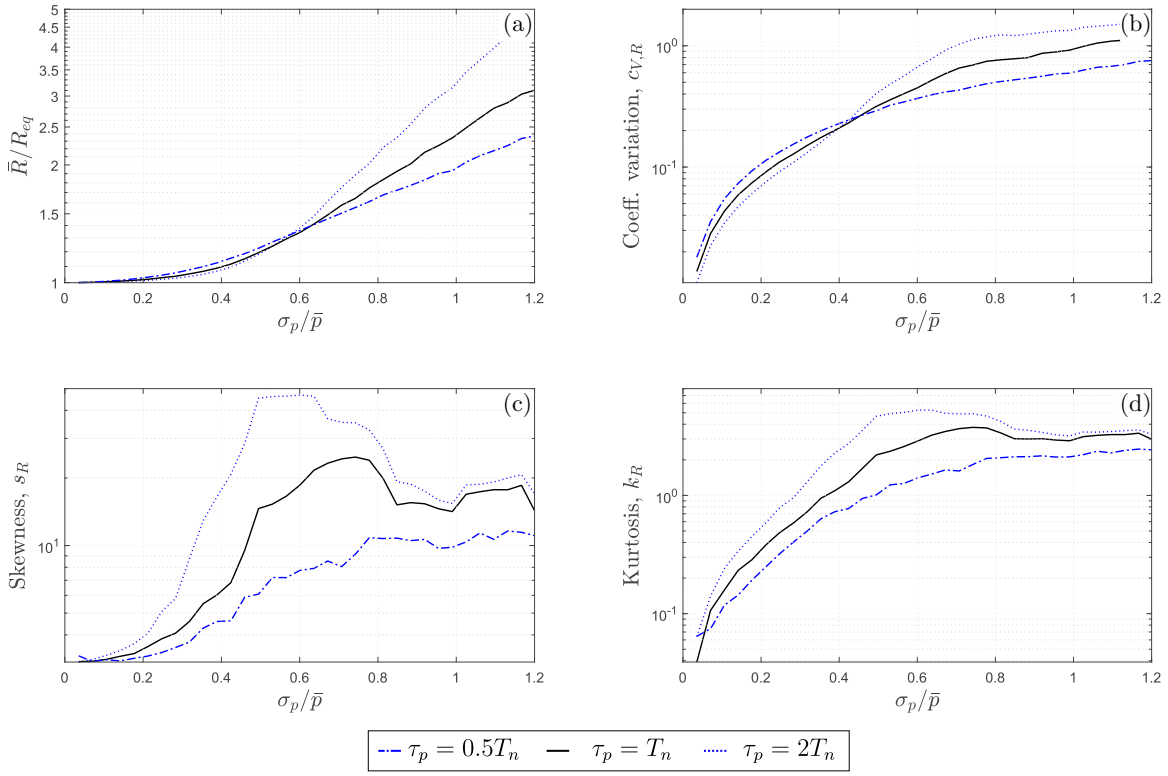

FIG. 4. Effect of $\sigma_p/\bar{p}$ on some relevant statistical parameters that describe the time-series $R(t)$.

higher than 0.4. Results on $R(t)/R_{\rm eq}$ are reported in Fig. 3. The noise intensities $\sigma_p/\bar{p} = 0.4$ and $\sigma_p/\bar{p} = 1.2$ [Figs. 3(d) and 3(e)] did not lead to inception of chaos: the radius time-series were very regular and exhibited fluctuations with the constant period T_n [Figs. 3(a) and 3(b)]. Differently, for $\sigma_p/\bar{p} = 2.0$ [Fig. 3(f)], a chaotic behavior of the bubble radius occurred [Fig. 3(c)].

The comparison of results shown in Fig. 2 (related to random forcing) and in Fig. 3 (corresponding to sinusoidal forcing) clearly shows that stochasticity promotes chaos inception. Although sinusoidal pressure signals have the same standard deviation [$\sigma_p/\bar{p} = 0.4$, Figs. 3(a) and 3(d)] or the same typical minimum values [Figs. 3(b) and 3(e)] of the stochastic forcing, sinusoidal pressure forcing does not lead to chaotic bubble dynamics, while random forcing does. Only the increment of the oscillation amplitude of the sinusoidal pressure to $A_p/\bar{p} = \sqrt{2} \times 2.0$ eventually leads to the inception of chaos. Namely, the noise intensity of the sinusoidal pressure should be five times larger than that of the stochastic case in order to observe a similar pattern of chaotic radius fluctuations.

The role of the correlation time of the forcing, τ_p, was also explored. Red dots in Figs. 2(a) and 2(b) correspond to $\tau_p = 0.5T_n$ and $\tau_p = 2T_n$, respectively; in each panel, data pertaining to $\tau_p = T_n$ (gray circles in both panels) are kept to allow for comparisons. It emerges that variations of τ_p are relevant only for $\sigma_p/\bar{p} \gtrapprox 0.30$ (i.e., above the threshold identified before) and positively correlated with the variability of the bubble radius. This behavior is in accordance with the physical explanation of the inception of chaos described so far. Higher values of correlation time of the forcing entail longer periods over which the pressure fluctuation has a constant sign. Hence, longer periods of pressure below average can be observed. These, in turn, promote large radius increments and thus the inception of chaos. This analysis is performed in more detail in Appendix A.

C. Statistical analysis

The analysis of Fig. 2 reveals that $R(t)$ deviates significantly from its equilibrium value and the behavior of $R(t)$ can be very irregular. To better quantify the deviations of $R(t)$ from $R_{\rm eq}$, the probability density functions (PDFs) and the cumulative distribution functions (CDFs) of the metric $R/R_{\rm eq}$ were evaluated. Details about this statistical analysis are given in Appendix B, where we report that changes in both $\sigma_p/\bar{p}$ and τ_p induce significant alterations in the PDF of the bubble radius $R(t)$. However, $\sigma_p/\bar{p}$ effects seem to be stronger. For this reason, the effect of $\sigma_p/\bar{p}$ was systematically explored in the relatively large range [0,1.20] for only three values of the noise correlation time $\tau_p = [0.5, 1, 2]T_n$.

For the sake of clarity, the corresponding effects on the PDFs of $R(t)$ are then expressed in terms of four relevant statistical parameters, reported in Fig. 4: (i) the mean value of the normalized bubble radius, $\bar{R}/R_{\rm eq}$; (ii) the coefficient of variation of $R(t)$, i.e., $c_{V,R} = \sigma_R/\bar{R}$; (iii) the skewness s_R of the time-series; and (iv) the kurtosis k_R of $R(t)$.

The noise intensity $\sigma_p/\bar{p}$ has a strong effect on the mean value of the bubble radius [Fig. 4(a)]. In particular, $\sigma_p/\bar{p}$ is positively correlated with $\bar{R}$. This is a key point: the mean value of the bubble radius depends not only on the mean pressure, $\bar{p}$, but also on the noise intensity, σ_p. Therefore, in

the case of a stochastic pressure forcing, it can be misleading to estimate the mean value of the bubble radius just from the mean (background) pressure.

When $\sigma_p/\bar{p}$ exceeds 0.60, different curves $\bar{R}/R_{\rm eq}$ are observed for different values of τ_p. This can be explained as follows. According to the analysis presented in Sec. III A, the deviation of $\bar{R}$ from $R_{\rm eq}$ is due to the nonlinear nature of the bubble dynamics, and, in particular, it is ascribable to the effect of time segments during which the instantaneous pressure is below average [i.e., when $p(t) < \bar{p}$]. When the pressure is below average, the bubble radius undergoes a strong increment and deviates significantly from $R_{\rm eq}$ [i.e., the equilibrium radius attained at $p(t) = \bar{p}$; see Figs. 2(c) and 2(d)]. This clearly contributes to an increase in $\bar{R}$. It was also pointed out that the higher τ_p is, the longer is the duration of time segments during which the instantaneous pressure is below average (see Appendix A), and thus the stronger are the increments of the bubble radius and, consequently, $\bar{R}$ from $R_{\rm eq}$. Besides $\bar{R}$, the other statistical parameters are all also strongly affected by the noise intensity [see Figs. 4(b)–4(d)].

The correlation time τ_p does not change the qualitative behavior of the curves presented in Fig. 4, however some peculiarities do occur: (i) the effect of τ_p on the mean value and on the coefficient of variation of $R(t)$ is most relevant for high values of $\sigma_p/\bar{p}$ [Figs. 4(a) and 4(b)]; (ii) the skewness and the kurtosis are affected by τ_p the most when $\sigma_p/\bar{p}$ is in the range [0.4,0.8] [see Figs. 4(c) and 4(d)], while instead the curves tend to merge for higher values of the correlation time of the pressure forcing.

The behavior of skewness and kurtosis shows other interesting aspects. For all investigated values of τ_p, they increase with increasing $\sigma_p/\bar{p}$ within the range $\sigma_p/\bar{p} = [0, 0.60]$. For $\sigma_p/\bar{p} \gtrapprox 0.60$, instead, they seem to tend monotonically (kurtosis) or nonmonotonically (skewness) to an asymptotic value [Figs. 4(c) and 4(d)]. Interestingly, the kurtosis tends to its Gaussian value of 3. In summary, the trends observed in Fig. 4 indicate that increments in the noise intensity tend to increase the mean radius of the bubble as well as the intensity of its variations [Figs. 4(a) and 4(b)]. The positive value of the skewness indicates that it is more probable to have $R(t) > R_{\rm eq}$ than $R(t) < R_{\rm eq}$. This asymmetry increases with increasing $\sigma_p/\bar{p}$ but saturates for $\sigma_p/\bar{p} \gtrapprox 0.60$. The behavior depicted by kurtosis indicates that the occurrence of extreme events (i.e., intermittency) in $R(t)$ increases with increasing noise intensity, but, as per the skewness, it saturates for $\sigma_p/\bar{p} \gtrless 0.60$.

An important aspect in studies about nonlinear oscillators is to evaluate whether the system behaves as a "damper" or as an "amplifier" of the external forcing [54]. To this end, the variability of the bubble radius was compared to the variability of the forcing pressure forcing (see Fig. 5). The gas bubble can be classified as a "damper" when the coefficient of variation of the fluctuating pressure forcing is larger than the coefficient of variation of the fluctuating bubble radius (i.e., $c_{V,p} > c_{V,R}$, gray zone in Fig. 5). On the other hand, if $c_{V,p} < c_{V,R}$ (white zone in Fig. 5), the gas bubble behaves as a noise "amplifier." The correlation time of the noise, τ_p, is a key parameter in determining the amplifier/damper behavior of the bubble oscillator. For $\tau_p \leqslant T_n$, the bubble dynamics usually exhibits

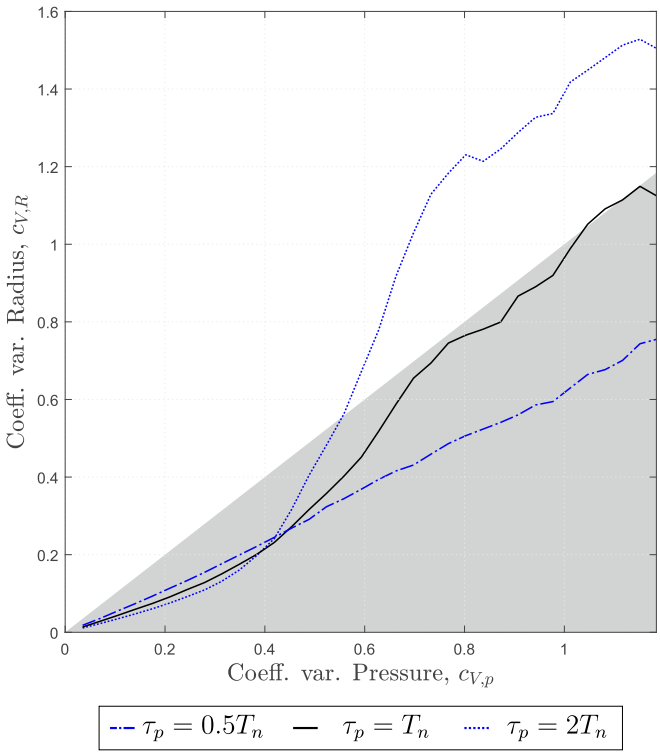

FIG. 5. Effect of the coefficient of variation of the pressure, $c_{V,p}$, on the coefficient of variation of the bubble radius, $c_{V,R}$. The shaded zone highlights the lower half-plane bounded by the bisector, where the bubble exhibits "damper" behavior. In the upper half-plane, the bubble behaves as an "amplifier."

a "damper" behavior. Differently, when $\tau_p = 2T_n$, the bubble behaves as a noise "amplifier" for $c_{V,p} \gtrapprox 0.5$.

D. Temporal correlation

It is now instructive to analyze the correlation timescale of the radius signal $R(t)$. To this end, we evaluate the autocorrelation function $\rho_R(t_l)$ [see the examples reported in Figs. 6(A1) and 6(B1)]. Then, we select the turnover time-lag $\hat{t}_{l,R}$ so that $\rho_R(\hat{t}_{l,R}) = 0.1$ [red circles in Figs. 6(A1) and 6(B1)]. Finally, the integral scale of the signal is evaluated as $I_R = \int_0^{\hat{t}_{l,R}} \rho_R(t_l) dt_l$. If the same procedure is applied to the time-series $p(t)$ [see Figs. 6(A2) and 6(B2)], the integral scale of the noise $I_p = \tau_p$ is obtained. To highlight the nonlinear behavior of the bubble oscillator, we focus on the ratio between the integral scale of the bubble radius and the integral scale of the pressure, namely I_R/I_p [Fig. 6(a)]. Note that the definition of the crossover timescale based on the fact that $\rho_R = 0.1$ is arbitrary. Note also that any other value of ρ_R reasonably close to 0 proved to lead to almost identical results and trends presented in Fig. 6(a), meaning that the results discussed in what follows are essentially independent of the exact definition of the crossover timescale.

Figure 6(a) shows the effect of the noise intensity $\sigma_p/\bar{p}$ on I_R/I_p, and two contrasting behaviors are observed. When the noise intensity $\sigma_p/\bar{p}$ is lower or greater than $\approx$0.30 (this value depends slightly on τ_p), then $I_R \ll I_p$ [gray zone in Fig. 6(a)] and $I_R \gg I_p$ [white zone in Fig. 6(a)], respectively.

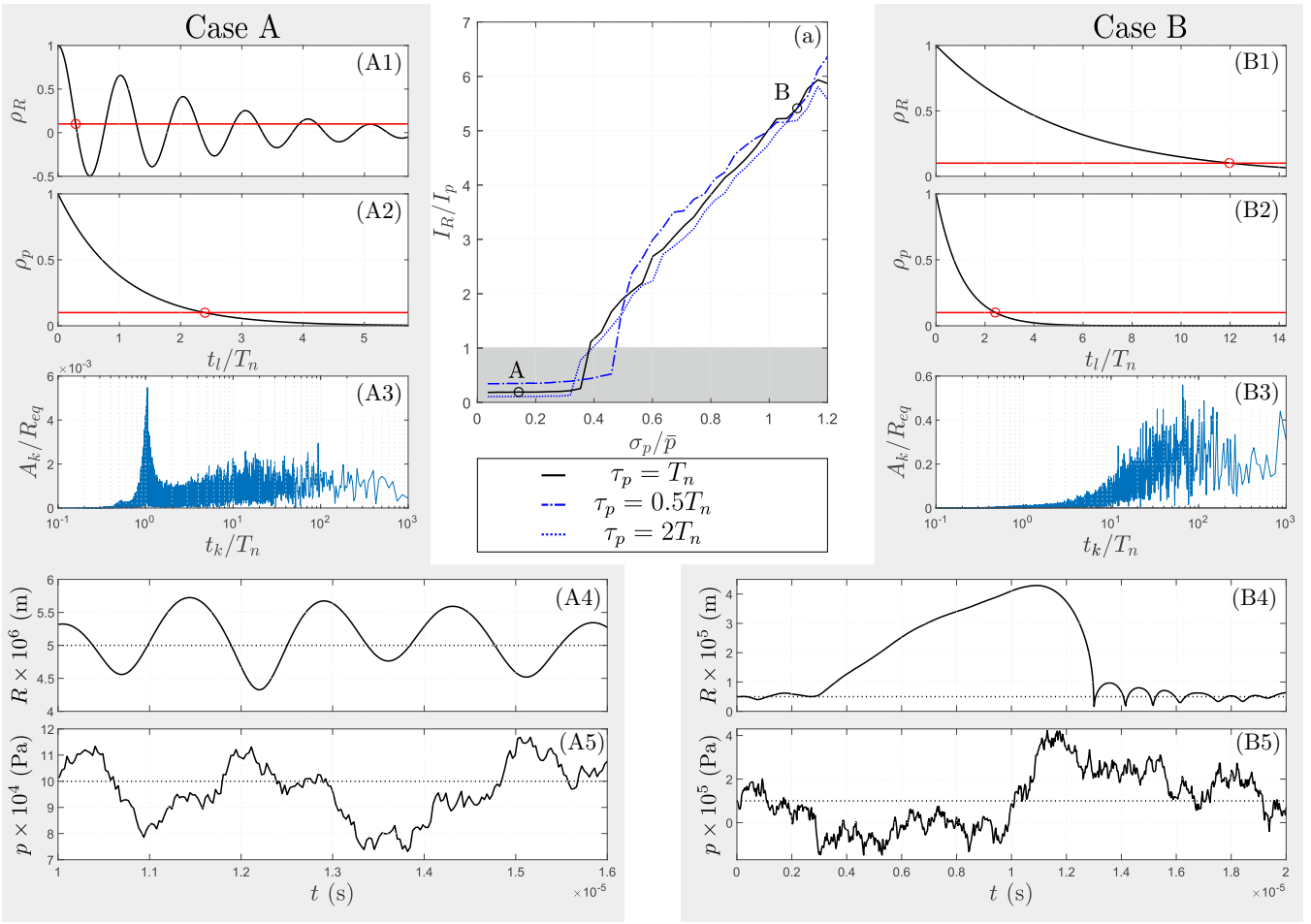

FIG. 6. (a) Effect of the noise intensity $\sigma_p/\bar{p}$ on the ratio between the integral scale of the radius time-series, I_R, and the integral scale of the pressure forcing, I_p. The gray zone highlights the condition $I_R < I_p$. Autocorrelation diagrams of $R(t)$ [panels (A1) and (B1)] and $p(t)$ [panels (A2) and (B2)]. The red lines mark the level where the autocorrelation function is 0.1. (A3),(B3) Power (amplitude) spectrum of $R(t)$. It should be noted that the horizontal axis reports the period of the kth harmonics (rather than its frequency). (A4)–(B5) Relevant time segment of the time-series $R(t)$ and $p(t)$. The dotted lines mark the equilibrium radius $R_{\rm eq}$ and the mean pressure $\bar{p}$.

To investigate the physical processes underpinning this sharp change in the behavior of I_R/I_p, we select two values of $\sigma_p/\bar{p}$ for which these contrasting behaviors are observed [see points A and B in Fig. 6(a)]. For both cases, the radius signal $R(t)$ [Figs. 6(A4) and 6(B4)] and the pressure signal $p(t)$ [Figs. 6(A5) and 6(B5)] are also reported over a significant time interval. Moreover, the power spectrum of $R(t)$ is evaluated [Figs. 6(A3) and 6(B3)].

Case A. For low values of the noise intensity, the only effect of pressure fluctuations is to excite the free oscillations of the bubble. For instance, when $\sigma_p/\bar{p} = 0.14$, the bubble radius oscillates with a varying amplitude [see Fig. 6(A4)], but the oscillation period is almost constant, and it is close to the natural period of oscillation of the bubble, T_n. This is confirmed by (i) the peak in the power spectrum of $R(t)$ [Fig. 6(A3)], and (ii) the shape of the autocorrelation function [Fig. 6(A1)], which resembles that of a periodic signal with period equal to T_n. Therefore, for low noise intensity levels, pressure variations are not able to significantly alter the free oscillations of the bubbles and induce chaos.

Case B. For high values of the noise intensity, pressure fluctuations drive the bubble dynamics. In the considered case (the noise intensity is $\sigma_p/\bar{p} = 1.10$), the bubble exhibits oscillations that attain large amplitudes [Fig. 6(B4)]. Differently from Case A, the oscillation period undergoes strong variations in the range $[0.5, 10]T_n$. As a result, the power spectrum of $R(t)$ [see Fig. 6(B3)] does not show any clear peak, and harmonics with periods in the wide range $[10^1, 10^3]T_n$ are characterized by comparable amplitudes. The signal portions reported in Figs. 6(B4) and 6(B5) show that pressure variations alter to a major extent the dynamics of the bubble—according to the physical mechanisms explained in Sec. III B—and free oscillations with period T_n are rarely observed. For instance, during the very long time segment from $t \approx 2 \times 10^{-6}$ to $t \approx 10 \times 10^{-6}$ s, the bubble radius becomes very large [≈ 10 times the equilibrium value; see Fig. 6(B4)]. After this long growth phase, oscillations with a period slightly higher than T_n are observed. The high values of I_R observed for high values of σ_p are therefore induced by the long periods over which a constant growth of $R(t)$ takes place. Note that these long-lasting growth phases are followed

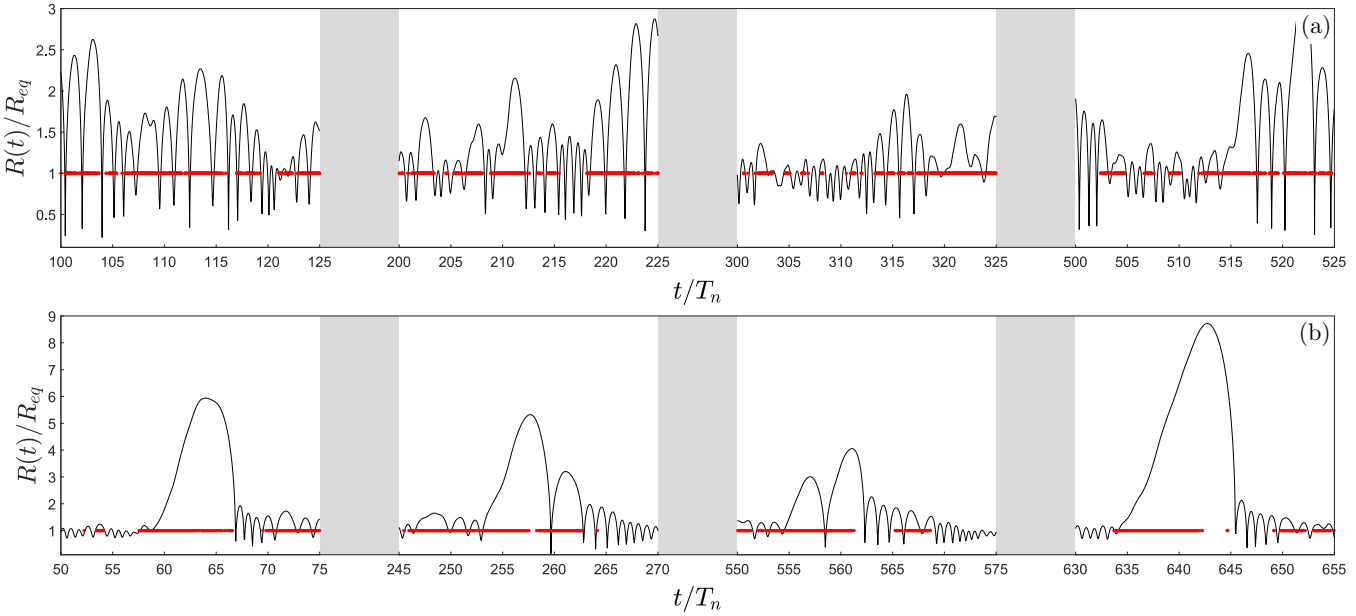

FIG. 7. Time-series of $R(t)/R_{\rm eq}$ in four relevant time segments in the case of $\tau_p = T_n/2$ (a) and $\tau_p = 2T_n$ (b). In both cases, $\sigma_p/\bar{p} = 0.70$. The red dots plotted at $R(t)/R_{\rm eq} = 1$ mark the instants when $p(t) < \bar{p}$, and they should not be confused with the dynamics of $R(t)/R_{\rm eq}$ reported by the black line. Panels (a) and (b) report different ranges in the vertical axis.

by rebounds exhibiting a period comparable to the bubble's natural period. It follows that the increment of I_R due to long-lasting radius growth phases cannot be balanced by phases during which the bubble oscillates with a period close to T_n.

The behavior previously described justifies the negligible effect of noise correlation time on bubble dynamics observed when the noise intensity is below the no-chaos/chaos threshold. This result was detected in Figs. 2(a) and 2(b)

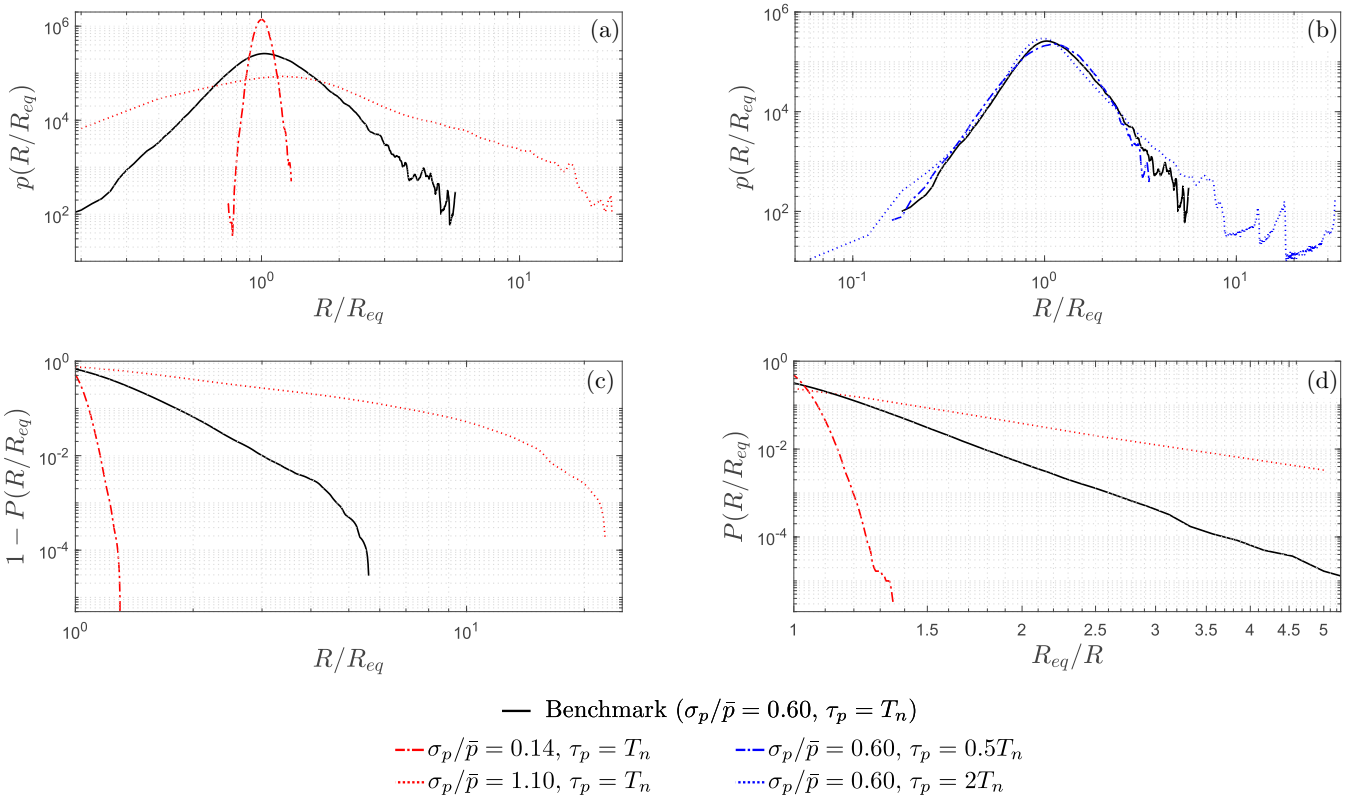

FIG. 8. (a,b) Probability density function of the metric $R/R_{\rm eq}$. (c) Complementary cumulative distribution function of $R/R_{\rm eq}$ evaluated for $R/R_{\rm eq} > 1$ (right tail of the distribution). (d) Cumulative distribution function of $R/R_{\rm eq}$ evaluated for $R/R_{\rm eq} < 1$ (left tail of the distribution); note that the horizontal axis reports $R_{\rm eq}/R$ and not $R/R_{\rm eq}$ as in panel (c).

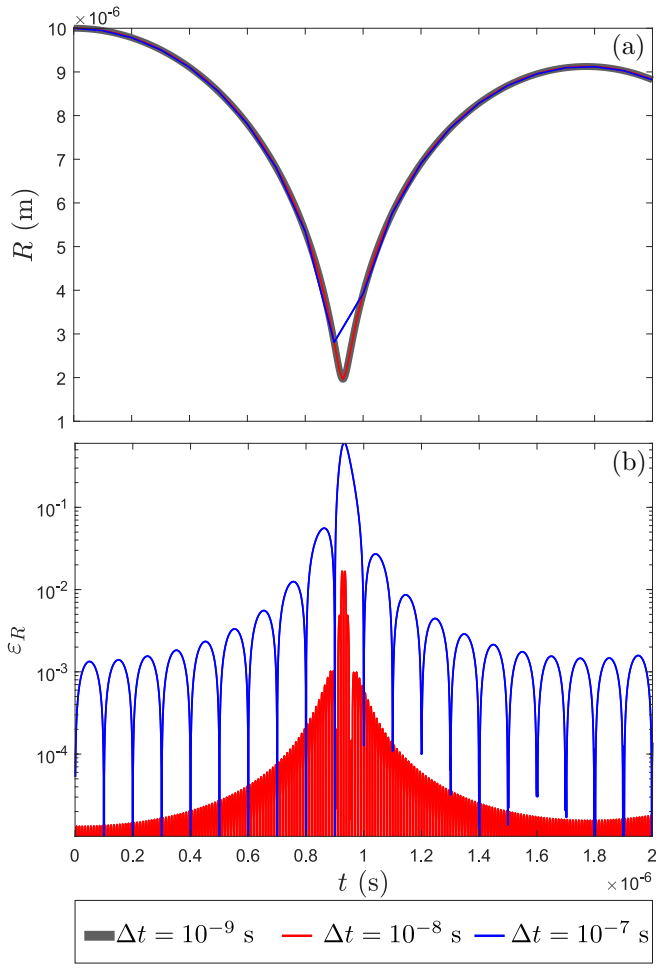

FIG. 9. (a) Example of curves $R(\Delta t, t)$ numerically computed adopting different time steps Δt. (b) Relative error $\varepsilon_R(t)$ occurring in the numerical computation performed with different time steps. The relative error is evaluated considering the curve computed with $\Delta t = 10^{-9}$ s as the exact reference. The initial conditions are $R(0)/R_{\text{eq}} = 2$ and $\dot{R}(0) = 0$. The pressure field is uniform.

(see Sec. III B). When the noise intensity is below the no-chaos/chaos threshold, bubbles oscillate at their natural frequency, and the only role of pressure fluctuation is to provide energy to sustain this motion. The characteristics of such pressure fluctuations are irrelevant in determining the frequency of vibration of the bubble. At most, they slightly alter the amplitude of the radius oscillation. Differently, when the noise intensity is above the no-chaos/chaos threshold, the bubble's dynamics are strongly driven by the pressure forcing. Hence, key characteristics of the pressure fluctuation—such as the noise correlation time—become important in determining bubble dynamics. In particular, longer correlation times—according to the mechanisms illustrated in Sec. III B—are associated with a more chaotic bubble response.

IV. CONCLUSIONS

The response of a single bubble to a stochastic pressure forcing was investigated. The motivation underpinning this study lies in the following: (i) the occurrence of random pressure fluctuations in many applications exploiting bubble dynamics; and (ii) the strong nonlinearities affecting the deterministic bubble dynamics, which suggests the possible occurrence of nontrivial noise-induced phenomena.

Two key parameters control stochastic bubble dynamics: the ratio between the standard deviation and the mean value of the forcing pressure ($\sigma_p/\bar{p}$), and the ratio between the noise correlation timescale bubble's free-oscillations period (τ_p/T_n). Two typical behaviors were detected. The first occurs when $\sigma_p/\bar{p}$ is lower than a threshold value around 0.3, namely, when pressure fluctuates with small amplitudes. In this case, the random pressure forcing mainly excites the free oscillations of the bubble whose radius undergoes small-amplitude oscillations and exhibits a rather regular periodicity. Moreover, we observed that (i) the effect of τ_p/T_n is small, (ii) the mean value of the background pressure can be adopted to estimate the mean value of the bubble radius, and (iii) the bubble always behaves as a damper of external noise.

The second behavior occurs when the fluid hosting the bubble experiences large-amplitude pressure fluctuations (i.e., $\sigma_p/\bar{p} > 0.3$). At these conditions, pressure stochasticity is able to trigger a chaotic bubble dynamics. Time-series of the bubble radius exhibit large-amplitude fluctuations and no evident periodicities occur, not even at the bubble's natural frequency. The parameter τ_p/T_n now significantly affects the bubble dynamics. In particular, when τ_p/T_n is high, long time intervals during which the instantaneous pressure is below the mean pressure appear; these intervals entail large increments of $R(t)$ and are usually followed by cavity collapses and rebounds. A strong variability of the $R(t)$ time-series occurs, and the bubble behaves as a nonlinear oscillator that amplifies the external noise. Consequently, the mean value of the background pressure cannot be adopted to estimate the mean value of the bubble radius; in doing so, the mean radius of the bubble can be underestimated by a factor 5. Finally, we should mention the key role of stochasticity in triggering chaos in a bubble's radius dynamics. Two pressure forcings—one stochastic, one sinusoidal—characterized by the same noise intensity $\sigma_p/\bar{p}$ behave very differently: the stochastic pressure forcing is more prone to trigger strong chaotic radius fluctuations than its sinusoidal counterpart.

In this work, we have demonstrated that stochastic forcing can induce interesting and unexpected bubble behaviors, presumably induced by the strongly nonlinear nature of the bubble oscillator. This paves the way to study other type of noises (e.g., dichotomous or shot noises) and to investigate how random forcing could be conveniently exploited in various applications. For example, noise-induced violent cavity implosions—attained when the intensity and correlation of pressure fluctuations are high—can be used to make water disinfection processes based on hydrodynamic cavitation and sono-chemical reactions more energy-efficient.

ACKNOWLEDGMENTS

R.V., C.M., and L.R. are grateful for the partial funding of this work provided by the European Union (Project BioEnPro4To POR FESR 2014/2020).

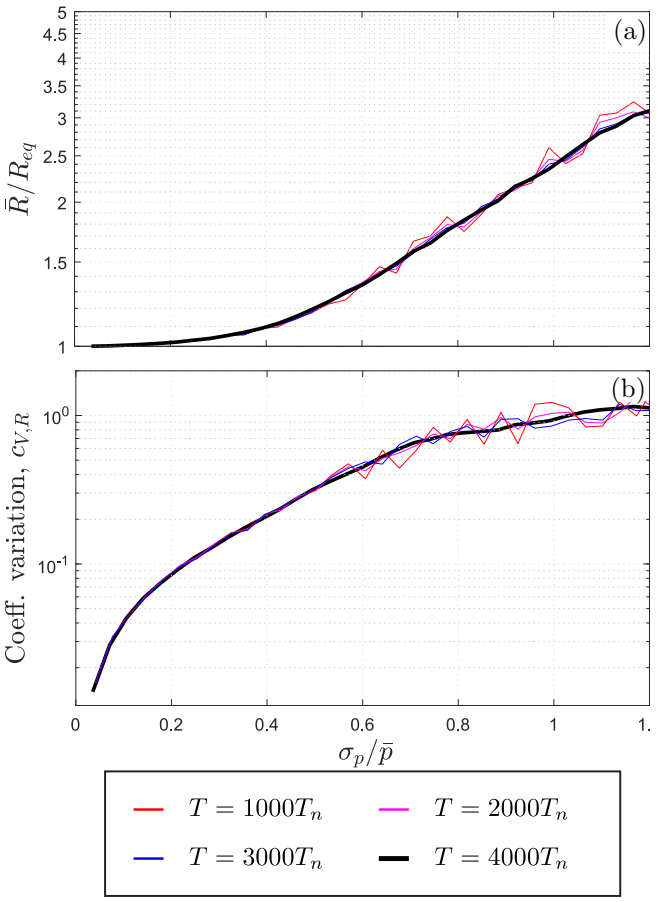

FIG. 10. Effect of the duration T of the simulation on the statistical metrics that describes the time-series $R(t)$. Similar to Fig. 4, two statistical parameters and their dependence on $\sigma_p/\bar{p}$ are considered. The different curves were evaluated considering different lengths of the simulation. The parameter $\tau_p = T_n$ is adopted.

APPENDIX A: ROLE OF CORRELATION TIME

To elucidate the increment of variability of $R(t)$ with τ_p, Figs. 7(a) and 7(b) report some exemplifying portions of time-series $R(t)/R_{\rm eq}$ obtained with the same noise intensity $\sigma_p/\bar{p} = 0.70$ (chosen in order to be in the chaos domain) but different noise timescales, namely $\tau_p = T_n/2$ and $\tau_p = 2T_n$, respectively. To relate the bubble radius dynamics to the pressure fluctuations, red dots plotted in Figs. 7(a) and 7(b) [along the line $R(t)/R_{\rm eq} = 1$] mark the instants when the instantaneous forcing pressure is below average [i.e., $p(t) < \bar{p}$]. From a physical point of view, when the instantaneous pressure is below average, the bubble radius tends to increase; on the contrary, radius contractions are promoted when the instantaneous pressure is above average [i.e., $p(t) > \bar{p}$, identified by no dots at $R(t)/R_{\rm eq} = 1$].

Figure 7(a) shows that, when the correlation time of the pressure forcing, τ_p, is low, time segments with pressure below average $[p(t) < \bar{p}]$ and time segments with pressure above average $[p(t) > \bar{p}]$ alternate fairly regularly: the red dots plotted at $R(t)/R_{\rm eq} = 1$ are grouped in short time segments, and they are followed by short segments where no dots are reported. A key consequence of short time segments with pressure below average $[p(t) < \bar{p}]$ is that the bubble radius cannot attain large increments [see the black time-series in Fig. 7(a)].

In contrast, for high values of the correlation time, time segments with pressure below average $[p(t) < \bar{p}]$ persist for a long time and are followed by long-lasting time intervals with pressure values above average $[p(t) > \bar{p}]$: Fig. 7(b) shows, indeed, that long sets of red dots alternate with long sets without dots. In this case, time segments in which the pressure is below average $[p(t) < \bar{p}]$ last so long that very large radius increments are attained [e.g., see the strong growth of $R(t)$ occurring at $t/T_n \approx 255$ in the second time segments of Fig. 7(b)]. Conversely, when the condition $p(t) > \bar{p}$ is restored, the bubble collapses. As explained in Sec. III B, the occurrence of these phases of remarkable radius expansion contributes to trigger the irregularity of $R(t)$.

APPENDIX B: STATISTICAL ANALYSIS—PDF AND CDF

In Fig. 8, we show some exemplifying cases in order to discuss the effect of $\sigma_p/\bar{p}$ and τ_p on the probability density function (PDF) and the cumulative density function (CDF) of the bubble radius. To this end, it is useful to define a benchmark case (see the thick black lines).

We selected the benchmark correlation time $\tau_p = T_n$. This choice was based on past studies that considered sinusoidal pressure oscillations. These studies found that complex dynamics occurs when the period of the sinusoidal forcing is equal to the natural oscillation period of the bubble [13,25,41,42,45]. Therefore, we expect bubbles to exhibit interesting dynamics when the correlation time of the noise signal is equal to the natural oscillation period of the bubble. On the other hand, we selected the benchmark noise intensity $\sigma_p/\bar{p} = 0.60$. This choice was based on the results reported in Figs. 2(a) and 2(b), showing chaotic dynamics of the bubble radius in the $\sigma_p/\bar{p}$ range [0.30,1.10]. We wanted to focus on bubbles exhibiting chaotic behavior, so we chose a value of noise intensity in this chaos range.

The noise intensity (in terms of $\sigma_p/\bar{p}$) was then altered, keeping $\tau_p = T_n$ [broken lines in Figs. 8(a), 8(c) and 8(d)]. Finally, τ_p was also changed while $\sigma_p/\bar{p}$ was kept at its benchmark value [broken lines in Fig. 8(b)]. The dotted (dash-dot) lines refer to a parameter higher (lower) than the benchmark value.

Irrespective of the noise parameters $\{\sigma_p/\bar{p}, \tau_p\}$, the quantity $R/R_{\rm eq}$ exhibits a unimodal PDF [Figs. 8(a) and 8(b)] whose shape, however, depends significantly on the noise intensity [Fig. 8(a)]. In particular, increments of $\sigma_p/\bar{p}$ induce the reduction of the peak height, the fattening of the tails, more asymmetrical PDFs, and the increment of the mode. Differently from $\sigma_p/\bar{p}$, changes of τ_p induce less relevant effects [Fig. 8(b)]. No changes of the peak height, of the mode of the PDF, and of the symmetry of the curves are in fact observed. The only relevant effect is a slight expansion of the distribution range toward higher values of $R/R_{\rm eq}$, which occurs when the correlation time increases [see the right tail of the dotted curve in Fig. 8(b)].

The tails are better described by the cumulative distribution functions. A complementary distribution is adopted to analyze the right tail [see Fig. 8(c)]. To focus on the left tail, the cumulative distribution is evaluated [see Fig. 8(d)]. Increments

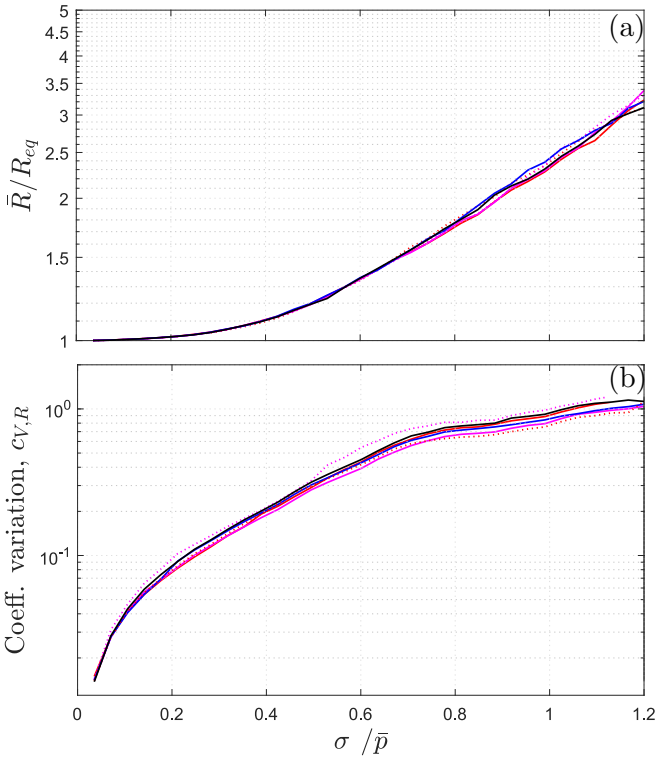

FIG. 11. Effect of different realizations of the stochastic process on the statistical parameters that describe the time-series $R(t)$. Similar to Fig. 4, two statistical parameters and their dependence on $\sigma_p/\bar{p}$ are considered. The different curves were evaluated with the same noise intensities and correlation times, but with a different set of random numbers. The parameter $\tau_p = T_n$ is adopted.

of the noise intensity mainly induce a fattening of the tails and an increment of the range [see Figs. 8(c) and 8(d)]. In the right tail, the range increases from 2 to 20 when $\sigma_p/\bar{p}$ increases from 0.14 to 1.10. Moreover, the frequency of occurrence of a given $R/R_{\rm eq}$ changes by orders of magnitude for the same increment of $\sigma_p/\bar{p}$. The same behavior is observed in the left tail: the minimum value attained by $R/R_{\rm eq}$ reduces from 0.6 to 0.2 when $\sigma_p/\bar{p}$ increases from 0.14 to 0.60. Interestingly, the further increment of $\sigma_p/\bar{p}$ from 0.60 to 1.1 does not lead to a reduction of $R/R_{\rm eq}$. The distribution does not extend beyond 0.2 [$R_{\rm eq}/R = 5$ in Fig. 8(d)]. However, the frequency of occurrence of this extreme value increases of more than one order of magnitude. Finally, as surmised from the analysis of Figs. 8(a) and 8(b), the PDFs of $R/R_{\rm eq}$ display asymmetry. In fact, the right tail is always characterized by a power-law behavior [linear in the log-log diagrams of Fig. 8(c)] for low values of $R/R_{\rm eq}$ followed by a cutoff. On the contrary, the left tail is always approximately linear [Fig. 8(d)].

APPENDIX C: NUMERICAL DETAILS

To evaluate the response of a gas bubble to a pressure forcing, the numerical integration of (1) is required. To this aim, the dimensional Eq. (1) is first made dimensionless adopting the length scale $R_{\rm eq}$ (i.e., the bubble radius in equilibrium conditions) and the time scale T_n [i.e., the period of bubble-free oscillations; see Eq. (5)]. Secondly, the second-order differential dimensionless equation is transformed in the system of two first-order differential dimensionless equations,

$$\tilde{y}_2 = \frac{d\tilde{y}_1}{d\tilde{t}},$$
$$\frac{d\tilde{y}_2}{d\tilde{t}} = \frac{\frac{p_w - p(\tilde{t})}{\mathcal{P}\tilde{y}_1} + \frac{\tilde{y}_2}{\mathcal{N}\tilde{y}_1}[p_G(1-3k) - p(\tilde{t}) + p_v] - \frac{1}{\mathcal{N}}\frac{dp(\tilde{t})}{d\tilde{t}} - \left(1 - \frac{\rm Ma}{3}\right)\frac{3\tilde{y}_2^2}{2\tilde{y}_1}}{1 - {\rm Ma} + \frac{4\mu}{\mathcal{M}\tilde{y}_1}}, \tag{C1}$$

where a tilde denotes dimensionless quantities, $\tilde{y}_1 = R/R_{\rm eq}$, ${\rm Ma} = \tilde{y}_2 R_{\rm eq}/cT_n$ is the Mach number, $\mathcal{P} = \rho R_{\rm eq}^2/T_n^2$, $\mathcal{M} = c\rho/R_{\rm eq}$, and $\mathcal{N} = \mathcal{M}/T_n$. Finally, p_w and p_G can be expressed, according to (2)–(4), in terms of $\tilde{y}_1$ and $\tilde{y}_2$ as

$$p_G = \left(\frac{2S}{R_{\rm eq}} - p_v + \bar{p}\right)\left(\frac{1}{\tilde{y}_1}\right)^{3k}, \tag{C2}$$
$$p_w = p_G + p_v - \frac{2S}{R_{\rm eq}\tilde{y}_1} - \frac{4\mu\tilde{y}_2}{T_n\tilde{y}_1}. \tag{C3}$$

The system of Eqs. (C1) was numerically solved by an explicit Runge-Kutta approach by using the Dormand-Prince pair [70].

To select the appropriate time step for numerical integration, a sensitivity analysis about this parameter was performed. The test case was a gas bubble with $R_{\rm eq} = 5$ μm, $R(0)/R_{\rm eq} = 2$, and $\dot{R}(0) = 0$ in a uniform pressure field. Three time steps ($\Delta t = [10^{-7}, 10^{-8}, 10^{-9}]$ s) were tested in the numerical simulations of the bubble dynamics (see Fig. 9). Figure 9(a) shows that $\Delta t = 10^{-9}$ and 10^{-8} s led to a bubble response [in terms of $R(t)$] that was indistinguishable, while $\Delta t = 10^{-7}$ s led to a less precise simulation of the system dynamics. To better quantify the quality of the numerical integrations, we evaluated the relative error

$$\varepsilon_R(t) = \frac{\|R(\Delta t, t) - R_{\rm ref}(t)\|}{R_{\rm ref}(t)}, \tag{C4}$$

where $R(\Delta t, t)$ is the bubble radius at the instant t evaluated with a numerical simulation in which the time step Δt was adopted. The term $R_{\rm ref}(t)$ is the "exact" reference value. In this case, we adopted $R_{\rm ref}(t) = R(\Delta t = 10^{-9}, t)$. The time step $\Delta t = 10^{-8}$ s was found suitable for the numerical integrations, as the maximum error $\varepsilon \sim 0.02$ was attained [see Fig. 9(b)].

To guarantee that the statistical description of a stochastic process was significant, two tests were performed. The first test concerns the duration of the considered stochastic process. In particular, we studied whether the same statistical values

were obtained, irrespective of the length of the analyzed time-series. Figure 10 reports the behavior of two statistical metrics as a function of $\sigma_p/\bar{p}$, as already discussed in Fig. 4. Each statistical index was evaluated from four time-series, $R(t)$, characterized by different durations, T. It can be observed that simulations carried out with $T > 2000T_n$ lead to curves characterized by the same behavior. The duration $T = 4000T_n$ was therefore deemed appropriate for the statistical analysis of the stochastic bubble dynamics.

The second test was to verify the independence of the results from a single realization, namely whether different stochastic realizations of the process lead to the same statistical indexes. Figure 11 reports two statistical parameters of Fig. 4. Each statistical index was evaluated with seven time-series, $R(t)$, characterized by a different pressure forcing. Each pressure time-series was characterized by the same statistics (σ_p, τ_p), but a different set of random numbers [see Eq. (7)] was adopted to introduce randomness. It can be observed that all simulations give curves characterized by the same behavior. Moreover, the mean value, the standard deviation, and the kurtosis of the bubble radius were basically the same.

[1] F. Risso, Agitation, mixing, and transfers induced by bubbles, Annu. Rev. Fluid Mech. **50**, 25 (2018).

[2] A. Prosperetti, Vapor bubbles, Annu. Rev. Fluid Mech. **49**, 221 (2017).

[3] C. Brennen, *Cavitation and Bubble Dynamics* (Cambridge University Press, Cambridge, 2013), pp. 1–249.

[4] M. Azmin, C. Harfield, Z. Ahmad, M. Edirisinghe, and E. Stride, How do microbubbles and ultrasound interact? Basic physical, dynamic and engineering principles, Curr. Pharm. Des. **18**, 2118 (2012).

[5] Y. Hao and A. Prosperetti, The effect of viscosity on the spherical stability of oscillating gas bubbles, Phys. Fluids **11**, 1309 (1999).

[6] J.-L. Laborde, C. Bouyer, J.-P. Caltagirone, and A. Gérard, Acoustic bubble cavitation at low frequencies, Ultrasonics **36**, 589 (1998).

[7] A. Prosperetti, The thermal behavior of oscillating gas bubbles, J. Fluid Mech. **222**, 587 (1991).

[8] L. Rayleigh, On the pressure developed in a liquid during the collapse of a spherical cavity, Philos. Mag. Ser. 6 **34**, 94 (1917).

[9] M. Plesset, The dynamics of cavitation bubbles, J. Appl. Mech. **16**, 277 (1949).

[10] F. R. Gilmore, The growth or collapse of a spherical bubble in a viscous compressible liquid, Technical Report No. 26-4, Hydrodynamics Laboratory, California Institute of Technology, Pasadena, CA, 1952.

[11] M. S. Plesset and A. Prosperetti, Bubble dynamics and cavitation, Annu. Rev. Fluid Mech. **9**, 145 (1977).

[12] A. Prosperetti, Bubble dynamics in a compressible liquid. Part 1. First-order theory, J. Fluid Mech. **168**, 457 (1986).

[13] W. Lauterborn and T. Kurz, Physics of bubble oscillations, Rep. Prog. Phys. **73**, 106501 (2010).

[14] H. Lin, B. Storey, and A. Szeri, Inertially driven inhomogeneities in violently collapsing bubbles: The validity of the Rayleigh-Plesset equation, J. Fluid Mech. **452**, 145 (2002).

[15] A. Moshaii and R. Sadighi-Bonabi, Role of liquid compressional viscosity in the dynamics of a sonoluminescing bubble, Phys. Rev. E **70**, 016304 (2004).

[16] O. Supponen, D. Obreschkow, and M. Farhat, Rebounds of deformed cavitation bubbles, Phys. Rev. Fluids **3**, 103604 (2018).

[17] M. Ghorbani, O. Oral, S. Ekici, D. Gozuacik, and A. Kosar, Review on lithotripsy and cavitation in urinary stone therapy, IEEE Rev. Biomed. Eng. **9**, 264 (2016).

[18] V. Agnese, V. Costa, G. Scoarughi, C. Corso, V. Carina, A. De Luca, D. Bellavia, L. Raimondi, S. Pagani, M. Midiri, G. Stassi, R. Alessandro, M. Fini, G. Barbato, and G. Giavaresi, Focused ultrasound effects on osteosarcoma cell lines, BioMed Res. Int. **2019**, 6082304 (2019).

[19] M. Dular, T. Griessler-Bulc, I. Gutierrez-Aguirre, E. Heath, T. Kosjek, A. Krivograd Klemenčič, M. Oder, M. Petkovšek, N. Rački, M. Ravnikar, A. Šarc, B. Širok, M. Zupanc, M. Žitnik, and B. Kompare, Use of hydrodynamic cavitation in (waste)water treatment, Ultrason. Sonochem. **29**, 577 (2016).

[20] A. Šarc, M. Oder, and M. Dular, Can rapid pressure decrease induced by supercavitation efficiently eradicate *Legionella pneumophila* bacteria?, Desalin. Water Treat. **57**, 2184 (2016).

[21] J. Carpenter, M. Badve, S. Rajoriya, S. George, V. Saharan, and A. Pandit, Hydrodynamic cavitation: An emerging technology for the intensification of various chemical and physical processes in a chemical process industry, Rev. Chem. Eng. **33**, 433 (2017).

[22] E. Burzio, F. Bersani, G. Caridi, R. Vesipa, L. Ridolfi, and C. Manes, Water disinfection by orifice-induced hydrodynamic cavitation, Ultrason. Sonochem. **60**, 104740 (2020).

[23] G.-F. Li, M.-Q. Cao, H.-L. Chen, and C.-Z. Ni, Modeling air gun signatures in marine seismic exploration considering multiple physical factors, Appl. Geophys. **7**, 158 (2010).

[24] Y. Liu, A.-M. Zhang, Z. Tian, and S. Wang, Investigation of free-field underwater explosion with Eulerian finite element method, Ocean Eng. **166**, 182 (2018).

[25] F. Hegedus and K. Klapcsik, The effect of high viscosity on the collapse-like chaotic and regular periodic oscillations of a harmonically excited gas bubble, Ultrason. Sonochem. **27**, 153 (2015).

[26] S. Popinet and S. Zaleski, Bubble collapse near a solid boundary: A numerical study of the influence of viscosity, J. Fluid Mech. **464**, 137 (2002).

[27] E. Zwaan, S. Le Gac, K. Tsuji, and C.-D. Ohl, Controlled Cavitation in Microfluidic Systems, Phys. Rev. Lett. **98**, 254501 (2007).

[28] Q. Wang, Multi-oscillations of a bubble in a compressible liquid near a rigid boundary, J. Fluid Mech. **745**, 509 (2014).

[29] A. A. Doinikov and A. Bouakaz, Theoretical model for coupled radial and translational motion of two bubbles at arbitrary separation distances, Phys. Rev. E **92**, 043001 (2015).

[30] Y. Fan, H. Li, J. Zhu, and W. Du, A simple model of bubble cluster dynamics in an acoustic field, Ultrason. Sonochem. **64**, 104790 (2020).

[31] C. Kling and F. Hammitt, A photographic study of spark-induced cavitation bubble collapse, J. Fluids Eng. Trans. ASME **94**, 825 (1972).
[32] I. Akhatov, O. Lindau, A. Topolnikov, R. Mettin, N. Vakhitova, and W. Lauterborn, Collapse and rebound of a laser-induced cavitation bubble, Phys. Fluids **13**, 2805 (2001).
[33] J. Rensen, D. Bosman, J. Magnaudet, C.-D. Ohl, A. Prosperetti, R. Tögel, M. Versluis, and D. Lohse, Spiraling Bubbles: How Acoustic and Hydrodynamic Forces Compete, Phys. Rev. Lett. **86**, 4819 (2001).
[34] A. Bergant, A. Simpson, and A. Tijsseling, Water hammer with column separation: A historical review, J. Fluids Struct. **22**, 135 (2006).
[35] A. Prosperetti, Bubble phenomena in sound fields: Part one, Ultrasonics **22**, 69 (1984).
[36] T. Leighton, From seas to surgeries, from babbling brooks to baby scans: The acoustics of gas bubbles in liquids, Int. J. Mod. Phys. B **18**, 3267 (2004).
[37] P. Kumar and A. Pandit, Modeling hydrodynamic cavitation, Chem. Eng. Technol. **22**, 1017 (1999).
[38] S. Arrojo and Y. Benito, A theoretical study of hydrodynamic cavitation, Ultrason. Sonochem. **15**, 203 (2008).
[39] W. Lauterborn, T. Kurz, R. Mettin, and C. Ohl, Experimental and theoretical bubble dynamics, Adv. Chem. Phys. **110**, 295 (1999).
[40] J. Keller and M. Miksis, Bubble oscillations of large amplitude, J. Acoust. Soc. Am. **68**, 628 (1980).
[41] W. Lauterborn and E. Cramer, Subharmonic Route to Chaos Observed in Acoustics, Phys. Rev. Lett. **47**, 1445 (1981).
[42] U. Parlitz, V. Englisch, C. Scheffczyk, and W. Lauterborn, Bifurcation structure of bubble oscillators, J. Acoust. Soc. Am. **88**, 1061 (1990).
[43] T. Leighton, Bubble population phenomena in acoustic cavitation, Ultrason. Sonochem. **2**, S123 (1995).
[44] G. Simon, P. Cvitanović, M. Levinsen, I. Csabai, and Á. Horváth, Periodic orbit theory applied to a chaotically oscillating gas bubble in water, Nonlinearity **15**, 25 (2002).
[45] C. Macdonald and J. Gomatam, Chaotic dynamics of microbubbles in ultrasonic fields, Proc. Inst. Mech. Eng. Part C: J. Mech. Eng. Sci. **220**, 333 (2006).
[46] V. Moholkar, S. Rekveld, and M. Warmoeskerken, Modeling of the acoustic pressure fields and the distribution of the cavitation phenomena in a dual frequency sonic processor, Ultrasonics **38**, 666 (2000).
[47] P. Kanthale, A. Brotchie, M. Ashokkumar, and F. Grieser, Experimental and theoretical investigations on sonoluminescence under dual frequency conditions, Ultrason. Sonochem. **15**, 629 (2008).
[48] Y. Zhang and Y. Zhang, Chaotic oscillations of gas bubbles under dual-frequency acoustic excitation, Ultrason. Sonochem. **40**, 151 (2018).
[49] T. Leighton, Transient excitation of insonated bubbles, Ultrasonics **27**, 50 (1989).
[50] K. Efthymiou, N. Pelekasis, M. Butler, D. Thomas, and V. Sboros, The effect of resonance on transient microbubble acoustic response: Experimental observations and numerical simulations, J. Acoust. Soc. Am. **143**, 1392 (2018).
[51] E. Igualada-Villodre, A. Medina-Palomo, P. Vega-Martínez, and J. Rodríguez-Rodríguez, Transient effects in the translation of bubbles insonated with acoustic pulses of finite duration, J. Fluid Mech. **836**, 649 (2018).
[52] N. Berglund and B. Gentz, *Noise-Induced Phenomena in Slow-Fast Dynamical Systems: A Sample-Paths Approach*, Probability and Its Applications (Springer, London, 2006).
[53] F. Sagués, J. M. Sancho, and J. García-Ojalvo, Spatiotemporal order out of noise, Rev. Mod. Phys. **79**, 829 (2007).
[54] L. Ridolfi, P. D'Odorico, and F. Laio, *Noise-Induced Phenomena in the Environmental Sciences* (Cambridge University Press, Cambridge, 2011).
[55] M. Freidlin, J. Szucs, and A. Wentzell, *Random Perturbations of Dynamical Systems*, Grundlehren der Mathematischen Wissenschaften (Springer, New York, 2012).
[56] W. McNamara III, Y. Didenko, and K. Suslick, Sonoluminescence temperatures during multi-bubble cavitation, Nature (London) **401**, 772 (1999).
[57] V. Moholkar and A. Pandit, Bubble behavior in hydrodynamic cavitation: Effect of turbulence, AIChE J. **43**, 1641 (1997).
[58] A. Sharma, P. Gogate, A. Mahulkar, and A. Pandit, Modeling of hydrodynamic cavitation reactors based on orifice plates considering hydrodynamics and chemical reactions occurring in bubble, Chem. Eng. J. **143**, 201 (2008).
[59] G. Uhlenbeck and L. Ornstein, On the theory of the Brownian motion, Phys. Rev. **36**, 823 (1930).
[60] A. Li and G. Ahmadi, Dispersion and deposition of spherical particles from point sources in a turbulent channel flow, Aerosol Sci. Technol. **16**, 209 (1992).
[61] P. Jung, Periodically driven stochastic systems, Phys. Rep. **234**, 175 (1993).
[62] E. Codling, M. Plank, and S. Benhamou, Random walk models in biology, J. R. Soc. Interface **5**, 813 (2008).
[63] A. Gu, B. Guo, and B. Wang, Long term behavior of random Navier-Stokes equations driven by colored noise, Discrete Contin. Dyn. Syst. Ser. B **25**, 2495 (2020).
[64] R. Mettin and A. Doinikov, Translational instability of a spherical bubble in a standing ultrasound wave, Appl. Acoust. **70**, 1330 (2009).
[65] H. Nazari-Mahroo, K. Pasandideh, H. A. Navid and R. Sadighi-Bonabi, Influence of liquid compressibility on the dynamics of single bubble sonoluminescence, Phys. Lett. A **382**, 1962 (2018).
[66] R. Löfstedt, B. P. Barber, and S. J. Putterman, Toward a hydrodynamic theory of sonoluminescence, Phys. Fluids **5**, 2911 (1992).
[67] E. Neppiras, Acoustic cavitation, Phys. Rep. **61**, 159 (1980).
[68] F. Hegedus, S. Koch, W. Garen, Z. Pandula, G. Paál, L. Kullmann, and U. Teubner, The effect of high viscosity on compressible and incompressible Rayleigh-Plesset-type bubble models, Int. J. Heat Fluid Flow **42**, 200 (2013).
[69] D. T. Gillespie, Exact numerical simulation of the Ornstein-Uhlenbeck process and its integral, Phys Rev E. **54**, 2084 (1996).
[70] J. Dormand and P. Prince, A family of embedded Runge-Kutta formulae, J. Comput. Appl. Math. **6**, 19 (1980).